Letters

Coupling-Insensitive Inductive Power Transfer System Driven by Single-Switch Inverter

Yifan Zhao, Yifan Jiang, Ziyang Xu, *Student Member, IEEE*, Haoyu Wang, *Senior Member, IEEE*, and Minfan Fu, *Senior Member, IEEE*

***Abstract*—This article is devoted to improving the coupling insensitivity of inductive power transfer (IPT) systems. Unlike previous studies that focused on establishing a stable source on the primary side (e.g., through a full-bridge inverter), this article leverages the load-sensitive characteristics of a single-switch resonant inverter to achieve a more stable system under varying coupling conditions. In addition, instead of designing the inverter and compensated coupler in a decoupled manner, the whole system is viewed as an ultrahigh-order resonant converter. Through simplification, the existing analytical inverter model is modified to fully explore the design potential for coupling-independent zero voltage switching and high robustness under parameter variations. The modified model also fills the gap in the holistic modeling of single switch IPT systems. In the experiment, a 60 W prototype is designed, when the coupling coefficient varies from 0.085 to 0.17, the output power maintains a fluctuation of 12%, with peak efficiency reaching 89.12%.**

***Index Terms*—Coupling insensitivity, detuned compensation, inductive power transfer (IPT).**

I. Introduction

In recent years, wireless inductive power transfer (IPT) has garnered widespread attention due to its ability to overcome the limitations of physical connections, offering a promising solution for future charging technologies. IPT systems with low to medium power ratings (below 100 W) are widely used in various applications such as smartphones, capsule robots, wearable devices, implantable biosensors and unmanned aerial vehicle (UAV) [1], [2], [3], [4], [5]. Unlike traditional charging that relies on wired connections, the greatest limitation of IPT lies in its coupling sensitivity. Especially in UAVs, the coupling coefficient often changes due to variations in coil position and environmental corrosion. This hinders its broader application. To effectively exploit the potential of IPT, it is crucial to design a system that is less sensitive to coupling variations [6], [7], [8], [9], [10], [11], [12].

There are several steady-state parameters that rely heavily on coupling, such as output power, voltage, and efficiency. To address various objectives, common methods include the design of passive networks or the control of active circuits. For example, active control can be utilized for stable output power. Passive approaches, on the other hand, involve the design of couplers, compensation networks, inverters, and rectifiers, which are often preferred because of their simplicity. Unlike traditional systems, modern strategies apply detuning techniques to the compensation network [6], [7], [8], [9]. This allows the net reactance of each resonant branch to offer increased design freedom, thereby reducing coupling or load sensitivity. Intuitively, when the primary side employs a load-independent inverter, it is more likely to maintain stable output on the secondary side under varying coupling conditions. Therefore, existing research has predominantly focused on designing the inverter as a stable voltage or current source (e.g., a full-bridge inverter and current source Class-E inverter), with an emphasis on the design of the compensation network. The primary side and secondary side of the system are treated as separate components, each optimized and designed independently. This approach fails to fully exploit the design freedoms of a complete IPT system.

Unlike bridge inverters, whose square output voltage is independent of load and can be seen as a voltage source. Traditional single-switch resonant inverters require specific resonant designs and are shown to be strongly load-sensitive. This article deviates from the traditional design philosophy. Instead of pursuing the establishment of a stable voltage source on the primary side, a detuned resonant inverter with detuned compensation is employed to achieve stable output on the secondary side under coupling variations. This article uses the simplest Class E inverter and series-series compensated coupler as examples to illustrate the design mechanism. An analytical time-domain model is also introduced to develop a coupling-insensitive output power system. Note that first, previous Class-E-based IPT systems have focused on configuring the Class-E as a constant voltage or current source (similar to a full-bridge inverter), the models often analyze the primary and secondary sides separately. Second, the previous Class-E analysis model only suit for resistive load [13], [14], [15]. In the proposed model, the

Received 26 March 2025; revised 3 June 2025; accepted 1 July 2025. Date of publication 29 July 2025; date of current version 21 November 2025. *(Corresponding author: Minfan Fu.)*

Yifan Zhao, Yifan Jiang, Haoyu Wang, and Minfan Fu are with the School of Information Science and Technology, ShanghaiTech University, Shanghai 201210, China, and also with Shanghai Advanced Research Institute, Chinese Academy of Sciences, Shanghai 201210, China (e-mail: fumf@shanghaitech.edu.cn; fuminfan@126.com).

Ziyang Xu is with the Department of Electrical and Computer Engineering, University of Texas at Austin, Austin, TX 78712 USA.

Digital Object Identifier 10.1109/TIE.2025.3587152

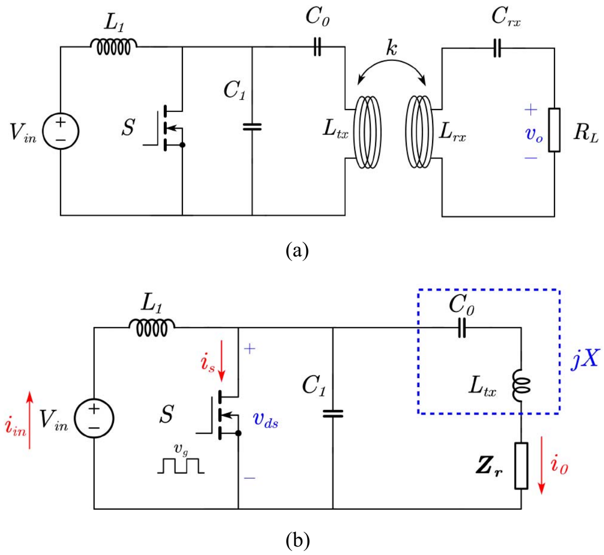

Fig. 1. Circuit model. (a) Original model. (b) Simplified model.

Class-E based IPT system is first viewed as an ultrahigh-order inverter with a reactive load. The proposed design also avoids parameter variation issues caused by components and nonlinear transistors, thereby dramatically improving system robustness. This design approach can be extended to achieve other coupling-insensitive features.

II. Coupling Insensitive Design

A. Analytical Model

Fig. 1(a) depicts the topology of a basic IPT system. V_{in} is the input voltage. S is the switch, whose duty cycle is D and frequency is f_s. The self-inductance L_{tx} of the transmitter (TX) coil resonates with C_0 at frequency f_s, exhibiting an additional reactance X

$$X = \omega_s L_{\text{tx}} - 1/(\omega_s C_0). \tag{1}$$

In contrast to the traditional Class E inverter, L_1 is utilized as a resonant inductor in place of a choke. The resonance frequency between L_1 and C_1 could be normalized with respect to ω_s, and a frequency factor q is then defined as follows:

$$q = 1/(\omega_s \sqrt{L_1 C_1}). \tag{2}$$

When the self-inductance of the receiver (RX) coil, L_{rx}, is not fully compensated by the capacitance C_{rx}, the resultant net reactance, in conjunction with the load resistance R_L, is reflected to the TX side via the mutual inductance $M(=kL_{\text{tx}}L_{\text{rx}})$. For ease of understanding, Fig. 1(b) illustrates the reflected impedance model of the IPT system, where $\boldsymbol{Z_r}$ is derived as follows:

$$\boldsymbol{Z_r} = R_r + jX_r = \frac{w_s^2 k^2 L_{\text{tx}} L_{\text{rx}}}{R_L + j\left(w_s L_{\text{rx}} - \frac{1}{w_s C_{\text{rx}}}\right)}. \tag{3}$$

In Fig. 1(b), i_{in}, i_o, and i_s denote the input current, output current, and the current through the switch S, respectively. v_{ds} represents the voltage across the switch. Provided that the quality factor of the output resonant tank is sufficiently high, the output current will exhibit a sinusoidal waveform, i.e.,

TABLE I
Parameters and Constraint Conditions of Design

Parameters	Value	Parameters	Value
L_1	15 μH	V_{in}	75 V
L_{tx}	140 μH	L_{rx}	50 μH
R_L	12.5 Ω	C_0	1.3 nF
C_1	4.9 nF	C_{rx}	3.012 nF
Q_{tx}	350	Q_{rx}	251

$$i_o(w_s t) = I_m \sin(w_s t + \phi). \tag{4}$$

The amplitude of the output current is represented by I_m, and ϕ denotes the initial phase shift relative to the gate signal.

The time-domain analysis of this inverter has been detailed in [15] and [16]. Through the intermediate variables q, p, and ϕ, the voltage across the switch is derived as follows:

$$\frac{v_{\text{ds}}(w_s t)}{V_{\text{in}}} = \Theta_1 \cos(q w_s t) + \Theta_2 \sin(q w_s t) + 1 - \frac{q^2 p}{1-q^2} \cos(w_s t + \phi) \tag{5}$$

where

$$\begin{cases} p = w_s L_1 I_m / V_{in} \\ \Theta_1 = -(\cos q\pi + q\pi \sin q\pi) \\ \qquad - \dfrac{qp}{1-q^2}[q \cos\phi \cos q\pi - (1-2q^2)\sin\phi \sin q\pi] \\ \Theta_2 = (q\pi \cos q\pi - \sin q\pi) \\ \qquad - \dfrac{qp}{1-q^2}[q \cos\phi \sin q\pi + (1-2q^2)\sin\phi \cos q\pi]. \end{cases} \tag{6}$$

The aforementioned model was initially employed for the design of a resonant inverter to achieve zero-voltage-switching (ZVS) and zero-derivative-switching (ZVDS) operation. These objectives establish two equality constraints that subsequently inform the parameter design process. In addition to the original design variables, such as L_1, C_1, and C_0, the compensation on the receiver side, and C_{rx}, is also introduced as a design parameter.

To ensure high efficiency, ZVS, is maintained by fulfilling the necessary conditions $v_{\text{ds}}(2\pi) = 0$. Incorporating this constraint into (5) correlates p, q, and ϕ in a single equation, as (7). ZVDS was not set as a mandatory condition to be taken into account, which provides greater design freedom

$$P = \zeta(q, \phi) = \frac{(1-q^2)(q\pi \sin q\pi - \cos q\pi + 1)}{q^2 \cos\phi \cos q\pi + (q - 2q^3)\sin\phi \sin q\pi + q^2 \cos\phi}. \tag{7}$$

It is worth noting that if the ZVDS constraint is incorporated, $\zeta()$ could potentially be solved [15], [16]. So, ZVDS was not set as a mandatory condition to be taken into account, which provides greater design freedom.

In Fig. 1(b), the switch voltage v_{ds} is filtered by the total impedance of jX and $\boldsymbol{Z_r}$. Consequently, upon applying the Fourier transform to v_{ds}, its sine and cosine components are,

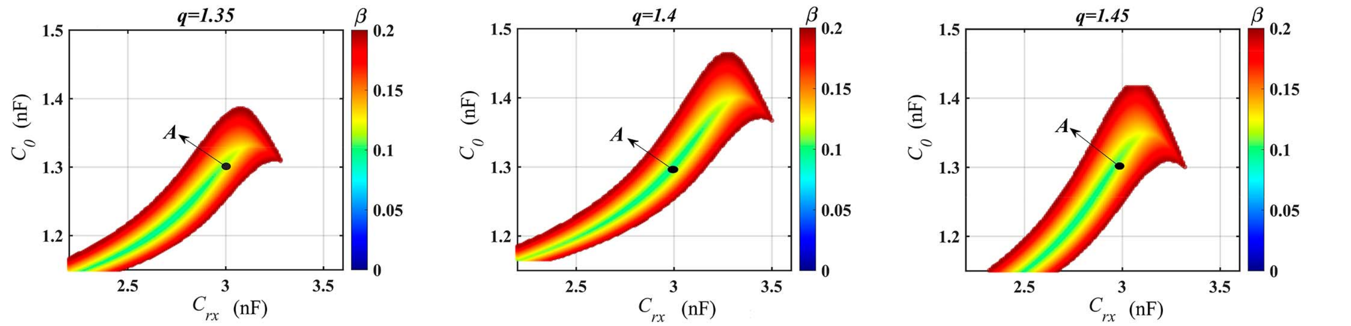

(a) (b) (c)

Fig. 2. Design candidate points. (a) $q = 1.35$. (b) $q = 1.4$. (c) $q = 1.45$.

respectively, applied to the resistive and reactive parts of the entire branch, i.e.,

$$\frac{X_r + X}{R_r} = \frac{\frac{1}{\pi}\int_0^{2\pi} v_{\mathrm{ds}}(w_s t)\cos(w_s t + \phi)}{\frac{1}{\pi}\int_0^{2\pi} v_{\mathrm{ds}}(w_s t)\sin(w_s t + \phi)}. \tag{8}$$

Since the previous formulas were all based on ϕ as an intermediate variable, we now need to express ϕ explicitly. By substituting (3), (5), and (7) into (8) yields an implicit expression of ϕ

$$\phi = \gamma(q, k, L_1, L_{\mathrm{tx}}, L_{\mathrm{rx}}, C_{\mathrm{rx}}, R_L, X). \tag{9}$$

Note that q, k, L_1, L_{tx}, L_{rx}, C_{rx}, R_L, and X represent all the circuit parameters.

Using the two implicit functions $\zeta()$ and $\gamma()$, the average input current I_{in} is derived as follows:

$$\begin{aligned} I_{\mathrm{in}} &= \frac{1}{2\pi}\int_0^{2\pi} i_{\mathrm{in}}(w_s t)\, dw_s t = \frac{I_m}{2\pi}\left(\frac{\pi^2}{2p} + 2\cos\phi - \pi\sin\phi\right) \\ &= \frac{V_{\mathrm{in}}\zeta(q,\gamma)}{2\pi w_s L_1}\left(\frac{\pi^2}{2\zeta(q,\gamma)} + 2\cos\gamma - \pi\sin\gamma\right). \end{aligned} \tag{10}$$

Since there are no energy-consuming components in the entire network except for the load. $P_o = P_{\mathrm{in}} = V_{\mathrm{in}} I_{\mathrm{in}}$, the output power is derived as follows:

$$P_{\mathrm{o}} = \frac{V_{\mathrm{in}}^2 \zeta(q,\gamma)}{2\pi w_s L_1}\left(\frac{\pi^2}{2\zeta(q,\gamma)} + 2\cos\gamma - \pi\sin\gamma\right). \tag{11}$$

B. Parameter Design

To better evaluate the performance of the system, it is crucial to adopt an objective and reasonable evaluation criterion. Here, we employ a universal standard for measuring power fluctuations [6]. When k varies within the range $[k_{\min}, k_{\max}]$, the corresponding output power would fluctuate within the bounds $[P_{\min}, P_{\max}]$. Define

$$\beta = (P_{\max} - P_{\min})/P_{\max} \tag{12}$$

$$\lambda = k_{\max}/k_{\min}. \tag{13}$$

The system should be designed to minimize β within a specified λ.

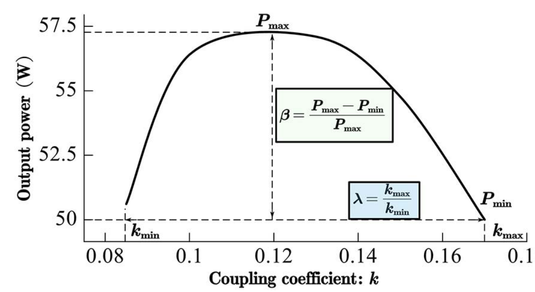

Fig. 3. k-Dependent power under proposed design.

Due to the complexity and implicit nature of the aforementioned models, numerical methods are required to assess the parameter design. Although q, k, L_1, L_{tx}, L_{rx}, C_{rx}, R_L, and X all influence the final performance, typically q, C_{rx}, and X are selected as the design variables while the inductive components are held constant. It should be noted that a change in q and X implies a corresponding change in C_1 and C_0, respectively. An example system is constructed based on the parameters listed in Table I. The frequency f_s is 400 kHz.

The derived model could computes all state variables from a given set of values of q, C_{rx}, and X. Subsequently, the power fluctuation rate β can be evaluated under various design variables. When q is set to 1.4, Fig. 2(b) illustrates the viable design points for different values of C_{rx} and X, with the color indicating β. Note that design points with $\beta > 20\%$ are excluded. A valley region is evident, and point A is selected from this region.

A high-order resonant converter must consider the resonance of the L_1&C_1, L_{tx}&C_o, and L_{rx}&C_{rx} branches. If the design objectives are highly dependent on perfect resonance, the system becomes too sensitive and difficult to maintain optimal operation in practice. The proposed system, however, does not need to achieve ideal resonance, significantly enhancing its robustness. For instance, taking into account potential variances in C_0 and C_{rx}, Point A in Fig. 2(b) is located in a valley region and remains stable even with a 5% variation in capacitance. Traditional inverters also face challenges due to nonlinear junction capacitance, which is represented by C_1. This study selected a transistor with a 200 pF capacitance at the target voltage level. When C_1 varies by 300 pF, q ranges from 1.35 to 1.45, yet Fig. 2(a) and (c) indicates that a low β is still achievable.

The point selection model does not account for the effects of ESR and the nonlinear junction capacitance. Therefore, additional

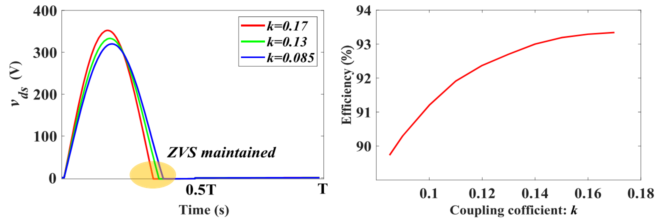

(a) (b)

Fig. 4. Simulation results. (a) v_{ds} at different k. (b) Efficiency.

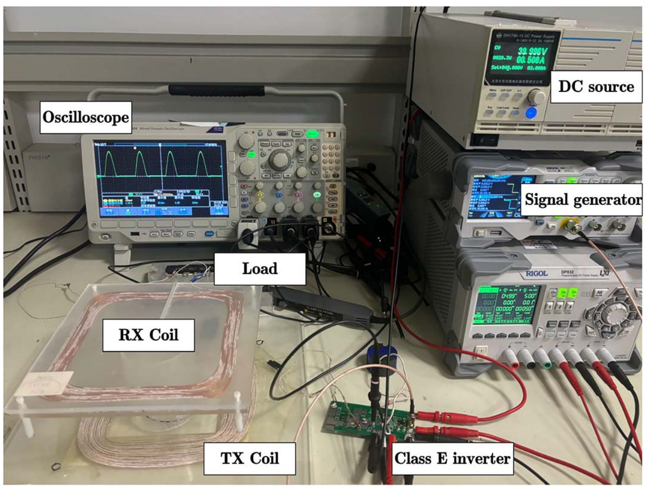

Fig. 5. Experimental setup.

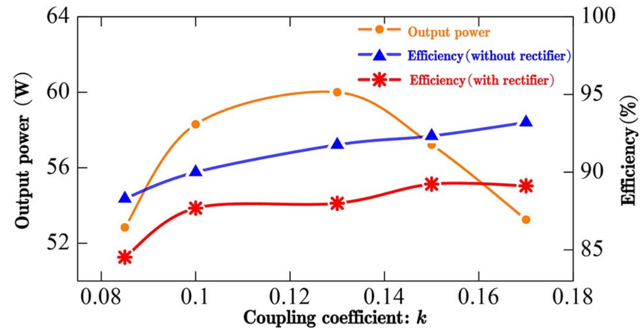

Fig. 6. Output power and efficiency.

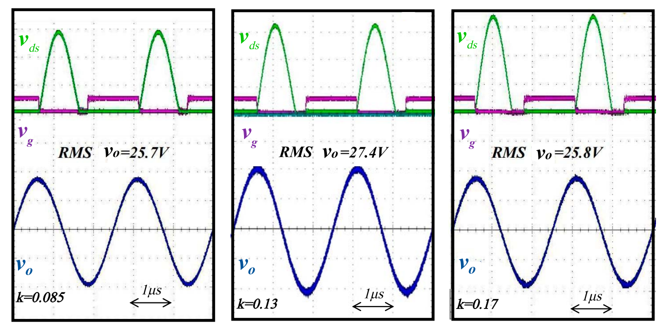

(a) (b) (c)

Fig. 7. Waveform at different k: v_g (2.5 V/div), v_{ds} (100 V/div), v_o (20 V/div). (a) $k = 0.085$. (b) $k = 0.13$. (c) $k = 0.17$.

validation through simulation is necessary to confirm the model's effectiveness. Using the parameters of Table I, the quality factors of the inductive components are taken into consideration, and the switch is modeled using a Spice model. Fig. 3 illustrates the relationship between output power and varying k. Showing the dynamic results of the system. It demonstrates that for k values less than 0.12, P_o increases with k, whereas for $k < 0.12$, P_o decreases with k. In this context, β is 12%. Meanwhile, in practical applications, the capacitance may vary with the dynamic operation of the system. In the experiments, both C_0 and C_{rx} are altered within a certain range, and the fluctuation rate of the output power remained around 12%.

Fig. 4 presents the waveform of the voltage across the switch v_{ds} and efficiency curves. Fig. 4(a) illustrates the coupling-independent ZVS operation. The switch voltage stress is maintained below 330 V. As depicted in Fig. 4(b), the efficiency progressively increases with k, reaching a peak efficiency of up to 93.6%.

III. Experimental Verification

An experimental IPT system, designed as previously described, is depicted in Fig. 5. Both the TX and RX coils are crafted from Litz wire, with specifications of 0.1 mm by 150 strands and a diameter of 1.7 mm. All system parameters are detailed in Table I. In alignment with design point A, the capacitors C_1, C_0, and C_{rx} are selected to be 4.9, 1.3, and 3.01 nF, respectively. High-precision, high-quality factor NP0/C0G ceramic capacitors are utilized. The system employs a GaN-based transistor (GS66508B). The isolated voltage probe (Tek TIVH08) and a high bandwidth current probe is used to measure the ac output and help calculate the power. The experiment is based on a transformer model and employs an impedance analyzer to measure the coupling coefficient k between two coils. By continuously adjusting the height, k between the two coils is altered.

It is important to note that a constant switch junction capacitance of 200 pF is taken into account and is to be incorporated into C_1.

Fig. 6 displays the measured output power and efficiency. The power fluctuation rate β is 12%, successfully aligning with the predictions made by the model-based design. In addition, the system efficiency augments with k, achieving a peak value of 89.12%. The typical waveforms for different coupling conditions

TABLE II
Comparison With Prior Works

Systems	k	λ	P_{max}	β	Efficiency	Switch
SS [9]	0.08–0.2	2.5	69 W	20%	66%–75%	4
LCC-S [7]	0.125–0.25	2	400 W	20%	88%–92%	4
X-type + S [8]	0.14–0.28	2	96 W	20%	83.5%–87.5%	4
Detuned SS [6]	0.07–0.15	2	163 W	20%	80.5%–93.5%	4
S/SP Wang et al. [17]	0.14–0.285	2	60 W	31%	81.55%–91.67%	2
S/T [18]	0.211–0.355	1.7	300 W	20%	86.8%–94.7%	4
S/SP Yao et al. [19]	0.1288–0.1733	1.3	200 W	6%	94.1%	4
PS/S [20]	0.2–0.6	3	63 W	67%	84.68%	4
LCL/LCL [20]	0.2–0.6	3	52 W	91%	88.6%	4
This article	0.085–0.17	2	60 W	12%	84.53%–89.12%	1

are also provided in Fig. 7. The inverter maintains ZVS and a stable output power throughout these conditions.

Table II presents a comparative analysis of the results in this article with previous works. The comparison encompasses various aspects, including topology, coupling range, λ, power level, β, efficiency, and the number of switches used. With a specified λ value of 2, the proposed system is capable of attaining the lowest β among the compared systems. In previous papers, bridge inverters were commonly employed, where coupling-insensitive power delivery was primarily achieved through the use of a detuned resonant tank. This paper demonstrates that a detuned resonant inverter, when integrated with a detuned tank, can further diminish the system's sensitivity to coupling variations with high robustness.

The operational ambient temperature range for the UAV spans from -40° C to 50° C. Experimental measurements demonstrate that the proposed system can withstand ambient temperatures up to 53° C, primarily determined by the temperature characteristics of the capacitors and transistors employed.

IV. Conclusion

This article explores the IPT system for the coupling-insensitive output power. A high-order system is constructed by integrating a resonant inverter with a tank. Contrary to the traditional approach of designing each component in isolation, all potential resonant elements are harnessed collectively to achieve high efficiency and a stable output. The existing model for an inverter has been modified to align with practical requirements. The model-based parameter design facilitates a swift assessment of the design region and system sensitivity. In the prototype system, as k fluctuates between 0.085 and 0.17, the power degradation rate is consistently maintained at 12%, with the peak efficiency reaching 89.12%. This approach effectively utilizes the load-sensitive of Class-E inverters within IPT systems, offering a significant level of efficiency and stability throughout the range of coupling variations.

References

[1] K. Nan et al., "An ingestible, battery-free, tissue-adhering robotic interface for non-invasive and chronic electrostimulation of the gut," *Nature Commun.*, vol. 15, no. 1, 2024, Art. no. 6749.

[2] D. Li et al., "Battery-free, wireless, and electricity-driven soft swimmer for water quality and virus monitoring," *Sci. Adv.*, vol. 10, no. 2, 2024, Art. no. peadk6301.

[3] T. Zheng, N. Kang, C. H. T. Lee, and L. Shao, "Wireless powered capsule robots with a wide locomotion range and random orientation via planar transmitting coils," *IEEE Robot. Autom. Lett.*, vol. 10, no. 3, pp. 2502–2509, Mar. 2025.

[4] S. Yao, X. Wang, J. Liang, H. Wang, and M. Fu, "A PV-battery three-port wireless charger for unmanned aerial vehicles," *IEEE Trans. Ind. Electron.*, vol. 72, no. 6, pp. 6564–6568, Jun. 2025.

[5] C. L. Kok, X. Fu, Y. Y. Koh, and T. H. Teo, "A novel portable solar powered wireless charging device," *Electronics*, vol. 13, no. 2, 2024, Art. no. 403.

[6] P. Zhao, J. Liang, H. Wang, and M. Fu, "Detuned LCC/S-S compensation for stable-output inductive power transfer system under ultrawide coupling variation," *IEEE Trans. Power Electron.*, vol. 38, no. 10, pp. 12342–12347, Oct. 2023.

[7] J. Zhao, T. Cai, S. Duan, H. Feng, C. Chen, and X. Zhang, "A general design method of primary compensation network for dynamic wpt system maintaining stable transmission power," *IEEE Trans. Ind. Electron.*, vol. 31, no. 12, pp. 8343–8358, Dec. 2016.

[8] H. Feng, A. Dayerizadeh, and S. M. Lukic, "A coupling-insensitive X-type IPT system for high position tolerance," *IEEE Trans. Ind. Electron.*, vol. 68, no. 8, pp. 6917–6926, Aug. 2021.

[9] H. Feng, T. Cai, S. Duan, X. Zhang, H. Hu, and J. Niu, "A dual-side-detuned series–series compensated resonant converter for wide charging region in a wireless power transfer system," *IEEE Trans. Ind. Electron.*, vol. 65, no. 3, pp. 2177–2188, Mar. 2018.

[10] J. Mai, A. Yang, Y. Wang, and D. Xu, "A parameter identification and control method based on compensation topology with strong misalignment tolerance," *IEEE Trans. Ind. Electron.*, vol. 71, no. 10, pp. 12173–12182, Oct. 2024.

[11] Y. Zhang, Y. Zhou, Y. Zheng, R. Xie, X. Chen, and X. Mao, "Dual-channel wireless power transfer systems with reconfigurable series-parallel switchers on both input and output ports for wide constant-voltage or constant-current range and misalignment tolerance," *IEEE Trans. Ind. Electron.*, vol. 72, no. 8, pp. 7974–7982, Aug. 2025.

[12] Y. Wang, J. Yang, K. Wang, and Y. Yang, "Highly integrated hybrid inductive and capacitive power transfer system with asymmetrical printed-circuit-board-based self-resonator," *IEEE Trans. Power Electron.*, vol. 40, no. 7, pp. 10254–10264, Jul. 2025.

[13] B. Li and K. Ngo, "Analysis and design of an isolated current source Class-E inverter with significant harmonics," *IEEE Trans. Power Electron.*, vol. 39, no. 11, pp. 14877–14887, Nov. 2024.

[14] M. Liu, M. Fu, and C. Ma, "Parameter design for a 6.78-MHz wireless power transfer system based on analytical derivation of Class E current-driven rectifier," *IEEE Trans. Power Electron.*, vol. 31, no. 6, pp. 4280–4291, Jun. 2016.

[15] S. Aldhaher, D. C. Yates, and P. D. Mitcheson, "Load-independent Class E/EF inverters and rectifiers for MHz-switching applications," *IEEE Trans. Power Electron.*, vol. 33, no. 10, pp. 8270–8287, Oct. 2018.

[16] A. Grebennikov and M. J. Franco, *Switchmode RF and Microwave Power Amplifiers*. New York, NY, USA: Academic, 2021.

[17] Y. Wang, J. Mai, Y. Yao, and D. Xu, "Analysis and design of an IPT system based on S/SP compensation with improved output voltage regulation," *IEEE Trans. Ind. Informat.*, vol. 16, no. 5, pp. 3256–3266, May 2020.

[18] J. Mai, Y. Wang, Y. Yao, and D. Xu, "Analysis and design of high-misalignment-tolerant compensation topologies with constant-current or constant-voltage output for IPT systems," *IEEE Trans. Power Electron.*, vol. 36, no. 3, pp. 2685–2695, Mar. 2021.

[19] Y. Yao, Y. Wang, X. Liu, K. Lu, and D. Xu, "Analysis and design of an S/SP compensated ipt system to minimize output voltage fluctuation versus coupling coefficient and load variation," *IEEE Trans. Veh. Technol.*, vol. 67, no. 10, pp. 9262–9272, Oct. 2018.

[20] J. Hou, Q. Chen, Z. Zhang, S.-C. Wong, and C. K. Tse, "Analysis of output current characteristics for higher order primary compensation in inductive power transfer systems," *IEEE Trans. Power Electron.*, vol. 33, no. 8, pp. 6807–6821, Aug. 2018.